RSC Advances

PAPER

View Article Online
View Journal | View Issue

Cite this: *RSC Adv.*, 2026, **16**, 20224

From *in silico* and machine learning model to validation: discovery of novel amide-functionalized imidazopyridines as PIM-1 kinase inhibitors using an integrated ligand and structure-based hopping approach

Vinayak Walhekar,[a] Shubham Dhadil,[a] Ankit Ganeshpurkar,[a] Srilakshmi Singagari,[b] Ayesha Begum Khadernaick,[c] Amol Muthal,[a] Vaibhav Shinde,[a] Ashwin Mali,[a] Raghavendra Kulkarni[d] and Ravindra Kulkarni *[a]

Pro-viral integration sites for Moloney murine leukaemia virus (PIM) kinases are the members of serine/threonine kinase family, that elevate cell division and inhibit apoptosis, thus making them as an attractive anticancer target. In this study, a virtual screening strategy based on a pharmacophore model was used to unearth imidazo[1,2-*a*]pyridin-2-yl phenyl benzamides as potential PIM1 inhibitors. A Python-based design workflow generated 27 candidate molecules, whose inhibitory activities were predicted using an in-house linear regression machine learning model. Selected compounds were synthesized, characterized, and subjected to cytotoxicity studies across multiple cancer cell lines, alongside assessments of PIM1 inhibition and apoptosis induction. Among the tested molecules, compound **6h** demonstrated the most promising antiproliferation activity in HT-29, PC3, and A549 cells, inducing apoptosis in HT-29 cells. It inhibited PIM1 kinase activity by 34.5% ± 3.4% at 10 μM and exhibited favorable *in silico* ADME and drug-likeness profiles, including high predicted absorption and absence of hepatotoxicity. These findings establish **6h** as a promising lead scaffold for the development of PIM1-1 targeted anticancer agents. The integration of pharmacophore modeling, machine learning prediction, and experimental validation highlights a viable strategy for accelerating kinase inhibitor discovery.

Received 20th January 2026
Accepted 19th March 2026

DOI: 10.1039/d6ra00514d

rsc.li/rsc-advances

1 Introduction

Cancer is identified as a menace to human beings among the plethora of diseases. In spite of huge investments, the fatal nature endures, with finite treatment outcomes. Despite huge efforts over decades on anticancer drug discovery, copious agents failed to eradicate tumor completely while maintaining minimal adverse effects and toxicity.[1,2] The modern era of anticancer drug discovery is based on dysregulating the function of kinases such as non-programmed proliferation and angiogenesis towards cancer cells.[3,4] Kinase drug discovery has led to a constellation of anticancer agents for the treatment of numerous cancers, among which serine/threonine and tyrosine classes of kinase are in the spotlight.[5]

PIM kinases are part of the serine/threonine kinase family, playing a vital role in cell proliferation and survival, followed by factors such as growth-factor-based activation of NF-κB and JAK/STAT, cytokines and stress.[6,7] PIM phosphorylates various pro-oncogenic proteins such as BAD, CDC25A/C, and 4EBP1 and thus is responsible for cell survival, progression, growth, oncogenesis and migration.[8] Alterations in the basic architecture of PIM kinases lead to the development of cancer. PIM-1, PIM-2 and PIM-3 kinases are mostly detected in solid and haematological malignancies (prostate, hepatocellular, and pancreatic tumours, acute myeloid leukaemia and multiple myeloma).[9–14]

The crystal structure of PIM kinases constitutes a unique hinge area, which is a part of the ATP binding motif, consisting of proline, which is not observed in other kinases. This unique structure provides a handle for the development of new inhibitors targeting PIM kinases.[15] All three isoforms of PIM kinases are structural analogues, but PIM-2 has a lower binding affinity (K_m: approx. 4 μM) for ATP than PIM-1 and PIM-3 kinases.[16] Multitudinous PIM kinase inhibitors have been documented in the past two decades, among which SGI-1776, AZD-1208, PIM447 and INCB053914 are potent pan-PIM kinase inhibitors[17–19] that have been put through the clinical pipeline but could not pass the trials

[a]*Department of Pharmaceutical Chemistry, BVDU'S Poona College of Pharmacy, Erandawane Pune-411038, Maharashtra, India. E-mail: ravigk2000@gmail.com*
[b]*Gitam School of pharmacy, Gitam University, Rushikonda, Visakhapatnam- 530045, India*
[c]*Shadan Women's College of Pharmacy, Khairabad, Hyderabad, India*
[d]*Department of Pharmaceutics, Sri Sanganabasava Mahaswamiji College of Pharmacy and Research Center, Vijayapura, Karnataka, India*

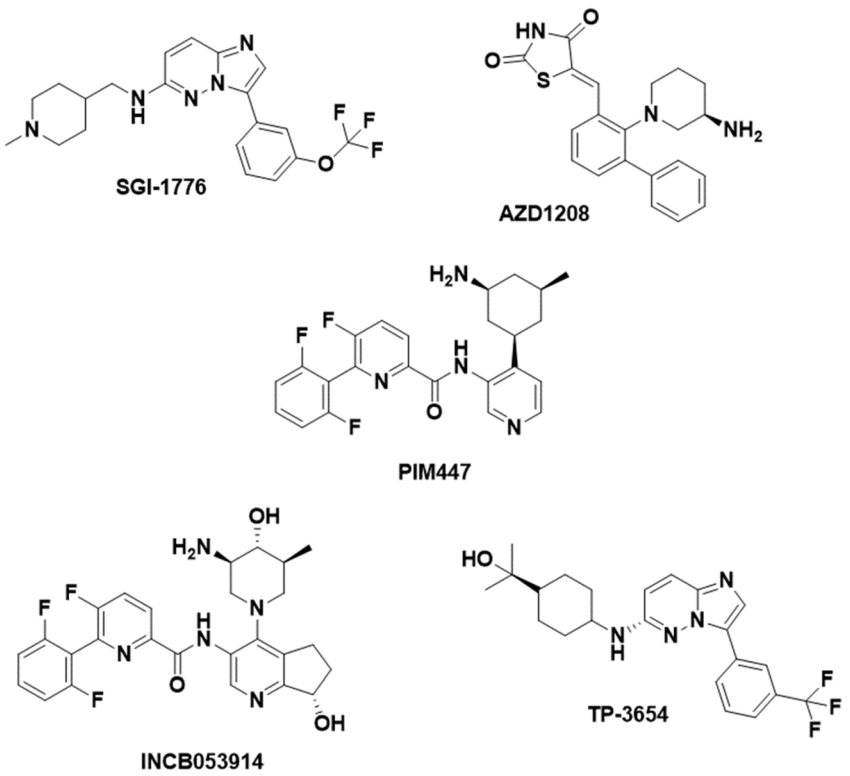

Fig. 1 Chemical structures of the documented PIM-1 kinase inhibitors.

due to persistant QTc prolongation, as shown in Fig. 1. Recently, a maximum number of ATP-competitive (Type-2) PIM kinase inhibitors have been developed instead of ATP mimetics due to their clinical significance, exemplified by TP-3654.[20]

Despite the numerous PIM1 kinase inhibitors explored in clinical trials, not a single molecule has been in clinical use in the treatment of cancer. Hence, this poses an enormous challenge for the discovery of new potential lead molecules. Our group has been consistently involved in exploring the structural information of kinases, especially PIM1, P38, GSK3β and EGFR and in searching for new kinase inhibitors using QSAR and machine leaning approaches.[21–27]

Numerous studies have explored computational tools for understanding the development of new PIM1 kinase inhibitors, including newer approaches like machine learning techniques. Such approaches eventually unearthed newer PIM1 kinase inhibitors, including some from natural sources.[28–30]

Recently, we applied a combination of computational approaches, in which a new lead was identified by pharmacophore and derivatized using the python/RdKit enumerator tool for analogues. A ML-based model predicted the PIM1 inhibitory activity of the molecules.[31] This research manuscript is in continuation of our efforts towards the development of kinase inhibitors, reporting one such series of molecules bearing the imidazo[1,2-*a*]pyridin-2-yl-phenyl benzamide scaffold, as potential PIM1 kinase inhibitors. The design strategy included a complex pharmacophore utility that identified the imidazopyridine scaffold, a Python script that generated twenty-seven new derivatives with appropriate substitution and a linear-regression-based ML model that predicted the activity, which was confirmed by molecular docking and dynamics simulation studies, as well as the *in vitro* PIM1 kinase inhibitory activity.[31]

2. Experimental section

2.1. Materials

All reagents and solvents were collected from commercial suppliers, including Sigma-Aldrich (Merck), Tokyo Chemical Industry (TCI), and Carbanio (India) and utilized as received without further purification. Synthetic procedures were conducted in carefully oven-dried borosilicate glassware. The reaction progress was checked *via* thin layer chromatography (TLC) using Silica Gel 60 GF254 plates, with visualization accomplished using UV light or iodine staining.

Compound characterization was performed as follows: The melting points were determined using a Veego VMP-PM digital machine and are presented as uncorrected. Infrared (IR) spectra were captured on a PerkinElmer FT-IR (ATR) spectrometer (results in cm^{-1}). Nuclear magnetic resonance (NMR) spectra (^1H at 500 MHz and ^{13}C) were acquired on a Bruker Avance III HD system using DMSO-d_6. Chemical shifts (δ) are cited in parts per million (ppm) in comparison to the solvent signal, with multiplicities designated as *s*, *d*, *t*, *q*, *m*, and br. Mass spectrometry (LC-MS/MS) using an Agilent Triple Quadrupole instrument was employed to confirm the identity of all intermediate and target molecules. Molecular modeling calculation studies were accomplished exclusively on desktops with the Windows 10 operating system, and molecular dynamics simulations were carried out on an Ubuntu 22.04 LTS desktop.

2.2. Pharmacophore-based virtual screening and machine-learning-based PIM1 kinase activity predictions

2.2.1. Pharmacophore postulate and database screening. The pharmacophore model involved strategic utilization of the co-crystallized ETP46546 molecule alongside PIM-1 kinase (PDB ID: 4A7C) in a LBDD-based ligand hopping approach. This approach led to the identification of unique features, which included aromatic rings, two hydrophobic and a hydrogen-bond acceptor. The features thus served as the foundational elements for the subsequent comprehensive pharmacophore model development. Validation of the developed pharmacophore model was executed through the Pharmit web server (https://.pharmit.csb.pitt.edu). A systematic search of the gigantic chemical space was undertaken using the Zinc15 library, covering an extensive compilation of 57,510,41 conformers of 74,763,522 chemical entities (accessed on 24/01/2023). The search protocol was meticulously designed to focus on a mono conformer per molecule, ensuring nuanced exploration of the chemical landscape. The search protocol was refined to encapsulate only one molecule per identified hit, thus optimizing the precision of the virtual screening process.[32]

2.2.2. Linear-regression-based ML model activity predictions. One of the hits recognized from the pharmacophore-model was further evaluated extensively in a Tanimoto coefficient similarity search by employing a Python script with SGI1776.[33] Further, the enumerator function in the Python script was explored for generating new monosubstituted analogues with a diversity of substituents. The generated structures were subjected to descriptor calculation using the RDKit package in Python, which generated descriptors, and an in-house developed LR-based ML model (separate models for type 1 and type 2, unpublished data from our research). The PIM1 kinase inhibitory activities were predicted for the designed and enumerated molecules. Few of the generated molecules were advanced to synthesis.

2.3. Method of synthesis

2.3.1. Synthesis of 2-(3-nitrophenyl)imidazo[1,2-*a*]pyridine (3). To a solution of 2-amino pyridine (5.2 g) (**1**) in acetonitrile (80 ml) was added 3-nitrophenacyl bromide (13.08 g) (**2**), and the reaction mixture was ultasonicated to dissolve the undissolved matter. Further, the solution was charged with sodium bicarbonate (5.6 g) and again ultrasonicated for 30 min. Upon completion, distilled water was added to the reaction mass and stirred for 15 min. The obtained yellow solid was filtered under vacuum. The yellow solid was purified by treatment with dilute HCl to yield a yellow crystalline solid, product (**3**); 11 g, yield: 85.60%, MP: 207–209 °C; FT-IR (cm^{-1}) (KBr) 3139 (heteroaromatic –CH stretch), 3079 (aromatic –CH stretch), 1635 (imine –C=N stretch), 1558 (-CH bending), 1520 (-NO_2 symmetric stretch), 1342 (-NO_2 asymmetric stretch), 717; ^{1}H NMR (500 MHz, DMSO) δ 8.51 (d, J = 7.8 Hz, 1H, amide N**H**), 8.23 (s, 1H Ar**H**), 7.54 (d, J = 9.0 Hz, 1H, Ar**H**), 7.28–7.18 (m, 2H, Ar**H**), 7.13–7.02 (m, 2H, Ar**H**), 6.87 (td, J = 6.7, 1.1 Hz, 1H, Ar**H**), 6.56–6.49 (m, 1H, Ar**H**); LC/MS: calculated $C_{13}H_9N_3O_2$ $[M+1]^+$: m/z 239.23; observed, 239.90 (deconvoluted).

2.3.2. Synthesis of 3-(imidazo[1,2-*a*]pyridin-2-yl)aniline (4). A mixture of 2-(3-nitrophenyl)imidazo[1,2-*a*]pyridine(1 g) (**3**), zinc granules (3 g) and concentrated HCl (8.2 ml) in deionized water (80 ml) was refluxed, and the progress of the reaction was monitored using TLC. The reaction mixture was diluted with deionized water and quenched by adding aqueous NaOH solution and then extracted with DCM three more times. The consolidated organic fraction was desiccated over anhydrous sodium sulfate and concentrated *in vacuo* to obtain the crude compound **4**, which was purified *via* column chromatography to yield the pure product **4**; 0.60 g, yield: 60%. Nature and colour: Light yellow crystalline solid; FT-IR (cm^{-1}) (KBr) 3324, 3292 (1° amine NH_2 stretch), 3202, 3128 (heteroaromatic –CH stretch), 3071 (aromatic –CH stretch), 1634 (imine –C=N stretch), 1608, 1585 (-CH bending), 744; ^{1}H NMR (500 MHz, DMSO) δ 8.51 (d, J = 7.8 Hz, 1H, Ar**H**), 8.23 (s, 1H, Ar**H**), 7.54 (d, J = 9.0 Hz, 1H, Ar**H**), 7.28–7.18 (m, 2H, Ar**H**), 7.13–7.02 (m, 2H, Ar**H**), 6.87 (td, J = 6.7, 1.1 Hz, 1H, Ar**H**), 6.56–6.49 (m, 1H, Ar**H**), 5.13 (s, 2H, N**H**$_2$); ^{13}C NMR (500 MHz, DMSO) δ 149.35 (Ar**C**NH$_2$), 145.67 (Ar**C**=N), 145.06 (Ar**C**), 134.85 (Ar**C**), 129.58 (Ar**C**), 127.20 (Ar**C**), 125.06 (Ar**C**), 116.97 (Ar**C**), 113.97 (Ar**C**), 113.95 (Ar**C**), 112.47 (Ar**C**), 111.70 (Ar**C**), 109.08 (Ar**C**); LC/MS calculated $C_{13}H_{11}N_3$ $[M+1]^+$: m/z 209.25; observed, 208.99 (deconvoluted).

2.3.3. General method for the synthesis of compounds (6a–r). A blend of 3-(imidazo[1,2-*a*]pyridin-2-yl)aniline (**4**) and triethylamine in anhydrous DCM was stirred at room temperature. The reaction mixture was charged drop-by-drop with substituted benzoyl chloride (**5a–r**). The resulting white suspension was stirred at room temperature for 5–8 h and was inspected over TLC for completion of the reaction. Upon completion, the precipitate of triethylamine hydrochloride was separated by filtration. The volatiles were concentrated under vacuum. The obtained residue was solubilized in DCM. The organic fraction was washed with saturated sodium bicarbonate solution three times, and the separated organic layer was dried over anhydrous sodium sulfate and concentrated *in vacuo* to yield the crude compounds (**6a–r**). The crude analogs were purified by column chromatography on silica gel to obtain off-white, white and yellow colored crystalline solids.

2.4. Biological assays

2.4.1. Materials and cell lines. Fetal bovine serum (FBS), the antibiotic solution, and Dulbecco's Modified Eagle's Medium (DMEM) were obtained from Gibco, Invitrogen and Thermofisher Scientific. Three cell lines, PC3, A549 and HCT-29, were obtained from NCCS, Pune, Maharashtra, India. Annexin V, propidium iodide, Alexa Fluor® 488 Annexin V/Dead Cell Apoptosis Assay Kit (cat no. – V1324), nuclease-free water (cat no. AM9932) were procurred from local vendors.

2.4.2. *In vitro* assays

2.4.2.1. Antiproliferative activity. The antiproliferative capabilities of the synthesized compounds were gauged using the MTT (3-(4,5-dimethylthiazol-2-yl)-2,5-diphenyl-2*H*-tetrazolium bromide) assay. In our previous publication, we reported that PIM-1 kinase expression was noted at elevated levels in carcinomas, including prostate, colon and lung cancers. Due to this

reason, human cancer cell lines such as PC3, HT29 and A549 were selected.[31] PC3, A549 and HCT-29 prostate, lung, and colon cancer cells, respectively, were cultured in 96-well plates using DMEM supplemented with 10% FBS. When the cell confluence was sufficient (up to 70%), the cells were treated with different concentrations of compounds, including the control, which contained DMSO for 24 h. The cells were washed with phosphate buffered saline after treatment with the compounds, and media aspiration was completed. In order to examine the viability of the cells, MTT was added (0.5 mg mL^{-1}) to each well and the MTT-treated cells were incubated at 37 °C for 4 h in a dark environment. Upon the completion of incubation, the MTT staining solution was removed and replaced with 200 μL of DMSO and the plates were shaken at 180 rpm for 10 minutes in order to make a clear solution, which facilitates the optical density measurement at 570 nm using a plate reader (**Benesphera 21**). To achieve better reliability of the activity data, this entire process was performed in triplicate before performing the statistical computations and visualization of the results.[34,35]

2.4.2.2. PIM-1 kinase inhibitory activity. The PIM-1 kinase inhibitory activity of the molecules was assessed using the luminescence-based ADP-Glo™ kinase Assay. The diluted enzyme, test compounds and ATP kinase buffer were transferred to a 384-well plate and incubated for 60 minutes. 5 μl of ADP-Glo™ reagent was also mixed into the wells and further incubated at RT for 40 minutes. Followed by the addition of ADP-Glo reagent, 5 μl of kinase detection reagent was added and incubated for 30 minutes, and the luminescence was recorded with a luminometer. Further, the % inhibition of the compounds was determined.[36]

2.4.2.3. Apoptosis assay employing Alexa Fluor® 488 Annexin V examination. Upon confluence of the HT-29 cells (70–80%), the cells were seeded in a sterile 12-well plate. The 24 h seeded cells were treated with the apoptosis-inducing agent (provided drugs) as per the provided drug concentrations, with half media change. A negative control was prepared by incubating the cells without the apoptosis-inducing agent. The treated cells were harvested by the trypsinization protocol and the harvested cells were properly washed with PBS. The washed cells were once again suspended in 1× Annexin binding buffer, further treated with Annexin V dye (2 μL) and subsequently incubated for 40 minutes at 2–8 °C. Post incubation, the test mixture with cells was centrifuged at 1500 rpm using 1*X* PBS for 5 minutes, and the cells were resuspended in PBS. Staining dye PI at 100 μg mL^{-1} was added just before sample acquisition on a flow cytometer and the samples were kept over ice. Apoptosis of the cells was assessed based on dye pigmentation on the flow cytometer. Annexin V detection was accomplished using an Attune Nxt flow cytometer with dual detection wavelengths at 488 nm with Ex/Em of 499/521. Ex/EM of 535/617 was employed for PI recognition. The green fluorescence of Annexin V-FITC/Alexa Fluor® 488 was recorded from the FITC channel (FL1 or

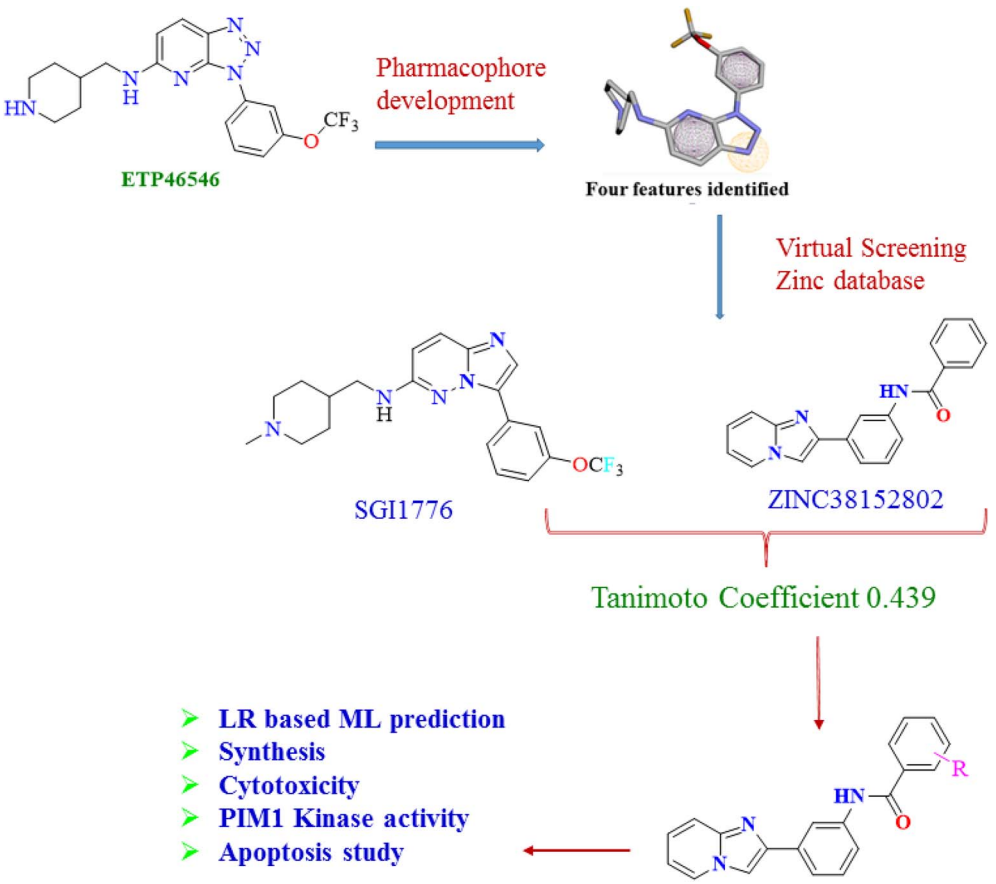

Fig. 2 Pharmacophore-based scaffold identification.

BL1), whereas the red fluorescence was detected from the PI channel (FL2 or BL2 or sometimes FL3 or BL3).[31,37]

2.5. Molecular modelling analysis

2.5.1. Molecular docking. Molecular docking analysis was used to explore ligand interactions with the amino acids that constitute the active site and ascertain the conformations that are vital for the stability of the resulting docked complexes. The molecular docking studies were executed employing AutoDock Vina module. The X-ray crystal structure was obtained from the RCSB Protein Data Bank (PDB ID: 4A7C, resolution: 2.30 Å).[38] Open source structure constructing tools were employed to draw the 2D structure of the molecules, which were converted into 3D structures using OpenBabel and minimized using MMFF94 with RdKit. Protein preparation was accomplished in AutoDockTools-1.5.6 and docking of the molecules was done with AutoDock Vina, adhering to established protocols.[39] The interaction efficiency between the compounds and the macromolecule was quantified in kcal mol^{-1}, the unit of expression recorded in the simulation studies' log file. PyMOL 2.1.1 and Discovery Studio Visualizer 2020 enabled graphical depiction of the small-molecule interactions with the macromolecules.[40]

2.5.2. Molecular dynamics simulation (MDS). MDS is one of the best and most well-appreciated computational methods for assessing the structural stability of small molecules. The docked pose of **6h** was considered for exploration of the complex stability using GROMACS 2020.1 with the CHARMM36 force-field to compute the protein parameters. Automated topology builder is one of the best supportive tools for generating the topology of ligands, and such generated topological parameters were complexed with the protein topology. MDS of the complex was performed under the NVT and NPT conditions, followed by minimization using the steepest algorithm after neutralization. The thus-generated structure was finally subjected to 100 ns MD simulation and post MD simulation analysis was performed. Various structural parameters of the simulated protein were analyzed, including the root mean square deviation (RMSD), radius of gyration, root mean square fluctuation, and hydrogen bond dynamics. PyMOL was employed to generate superimposed poses for comprehensive visualization of the molecular dynamics trajectories.[31,41,42]

2.5.3. ADME and drug-likeliness prediction. Assessment of the ADMET profile and drug-likeliness is indispensable for decisive identification of the potential of a chemical compound as a viable drug candidate. In the present study, the online software Swiss ADME and pkCSM-pharmacokinetics were used to predict the ADMET features and evaluate Lipinski's Rule of Five.[43,44]

3 Results and discussion

3.1. Molecule hybridization

In the past few decades, plentiful PIM kinase inhibitors have been discovered, including SGI-1776 and AZD-1208, which were found to possess potent PIM kinase inhibitory strength but failed due to an unavoidable cardiac toxicity profile for SGI-1776 in the clinical trial phase-1. The design of imidazopyridine amides was based on multiple approaches involving pharmacophore and database search, ML activity prediction and evaluation of the scaffold hopping attributes using molecular docking and MD simulations.

Table 1 Details of ML statistical data

Type	Iteration	R^2	Predicted R^2	Q^2
DFG in	121	0.912 683	0.742 594	0.549 658
DFG in	1080	0.910 914	0.761 765	0.533 005
DFG out	871	0.929 642	0.740 439	0.63
DFG out	2018	0.908 237	0.812 169	0.61

3.2. Pharmacophore postulate and database virtual screening

ETP46546 is a PIM-1 kinase inhibitor with an IC_{50} of 6 nM for type-2/ATP non-competitive inhibition. It constitutes the 1,2,3-triazolo [4,5-*b*]pyridine and piperidine rings vital for selective PIM-1 kinase inhibition, which was enhanced by substitutions of the alkyl functionalities affixed to the phenyl ring. We derived four featured pharmacophores, namely aromatic rings (A), two hydrophobic interactions, and a hydrogen bond acceptor (HA), as depicted in Fig. 2. Furthermore, the established pharmacophores were queried against the ZINC15 database using the Pharmit server to determine

Table 2 Predicted PIM1 kinase inhibitory potentials of enumerated molecules

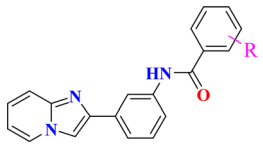

Position	Substituent	DFG In	DFG out
2	C	7.50	5.50
2	OC	7.14	5.62
2	Cl	7.48	5.38
2	F	7.30	5.37
2	N	6.69	5.40
2	C(F)(F)F	6.96	5.44
2	OC(F)(F)F	6.60	5.61
2	c1ccc2ccccc2c1	8.28	5.37
2	Br	6.00	5.98
3	C	7.48	5.50
3	OC	7.14	5.65
3	Cl	7.48	5.43
3	F	7.30	5.40
3	N	6.67	5.43
3	C(F)(F)F	6.94	5.47
3	OC(F)(F)F	6.60	5.64
3	c1ccc2ccccc2c1	8.28	5.37
3	Br	6.00	6.01
4	C	7.49	5.50
4	OC	7.14	5.65
4	Cl	7.48	5.43
4	F	7.30	5.40
4	N	6.67	5.43
4	C(F)(F)F	6.94	5.47
4	OC(F)(F)F	6.60	5.64
4	c1ccc2ccccc2c1	8.28	5.37
4	Br	6.00	6.01

the virtual hits. Fifteen thousand hits were filtered from the database, with numerous aromatic and heterocyclic scaffolds, namely, tetrahydrobenzothiophene, imidazopyridine, benzothiophene and others. They were sorted based on the score, from which ZINC38152802 was identified, with a score of −9.21 kJ mol^{-1}, which was encouraging as compared to the other hits.[31]

3.3. Similarity search

In order to verify the pharmacophore search and resultant molecule ZINC38152802, Tanimoto similarity and fingerprint search were performed by running an in-house Python script. Such similarity search has been successfully applied by us, which enhanced the confidence towards selecting these molecules.[31] The comparison was accomplished against SGI1776, a known inhibitor with a PIM1 kinase inhibitory activity of 7 nM. The Tanimoto similarity determined by using MACCS keys with 166 bits had a moderate similarity coefficient of 0.439. This moderate similarity suggests approximately 44% substructural common features between ZINC38152802 and SGI1776.

3.3.1. Linear-regression-based machine learning activity prediction. An attempt was made to develop ML models by considering fifty-eight and forty-eight molecules for the type 1 and type 2 models. Numerous ML models, including RF, LR and DT, have been developed for PIM kinase1 DFG in and DFG out inhibitors. Among the generated models, LR models for both DFG in and DFG out were identified to be statistically best and robust, and hence these models were considered for the predictions, as listed in Table 1.[37]

Previously, we reported the development of QSAR models in support of structure-based docking and molecular dynamics simulation[21] for predicting the activity of new molecules based on the ML model. In continuation of our previous research developments [unpublished data from our research], a Python script was executed by feeding SMILE strings of ZINC38152802, and monosubstitution was assigned on the 2nd, 3rd and 4th positions of the phenyl group of the amidic bridge, which generated twenty-six new analogues.[31] The descriptors for the enumerated molecules were generated using the RdKit module, and the required descriptors were selected. The predicted activities of the enumerated molecules have were determined by employing the models listed in Table 1, and the ML-predicted activities are summarized in Table 2.

3.4. Discrimination of PIM-1 kinase inhibitors (Type-2) postulated by a structure-based molecule design strategy

Triazolopyridines constituting PIM-1 kinase inhibitor ETP46546 with an IC_{50} of 6 nM were the input for the development of the pharmacophore, which eventually identified ZINC38152802 as a new hit. ZINC38152802 was further derivatized and twenty-five such analogs were designed. These twenty-five molecules were docked within the crystal structure of PIM-1 kinase (PDB ID: 4A7C), from which eighteen molecules demonstrated affirmative binding interactions comparable to that of ETP46546.[31] All eighteen molecules interacted through hydrogen interactions with Lsy67, Asp128 and Asp186 of the binding pocket of PIM-1 kinase, as depicted in Fig. 3.

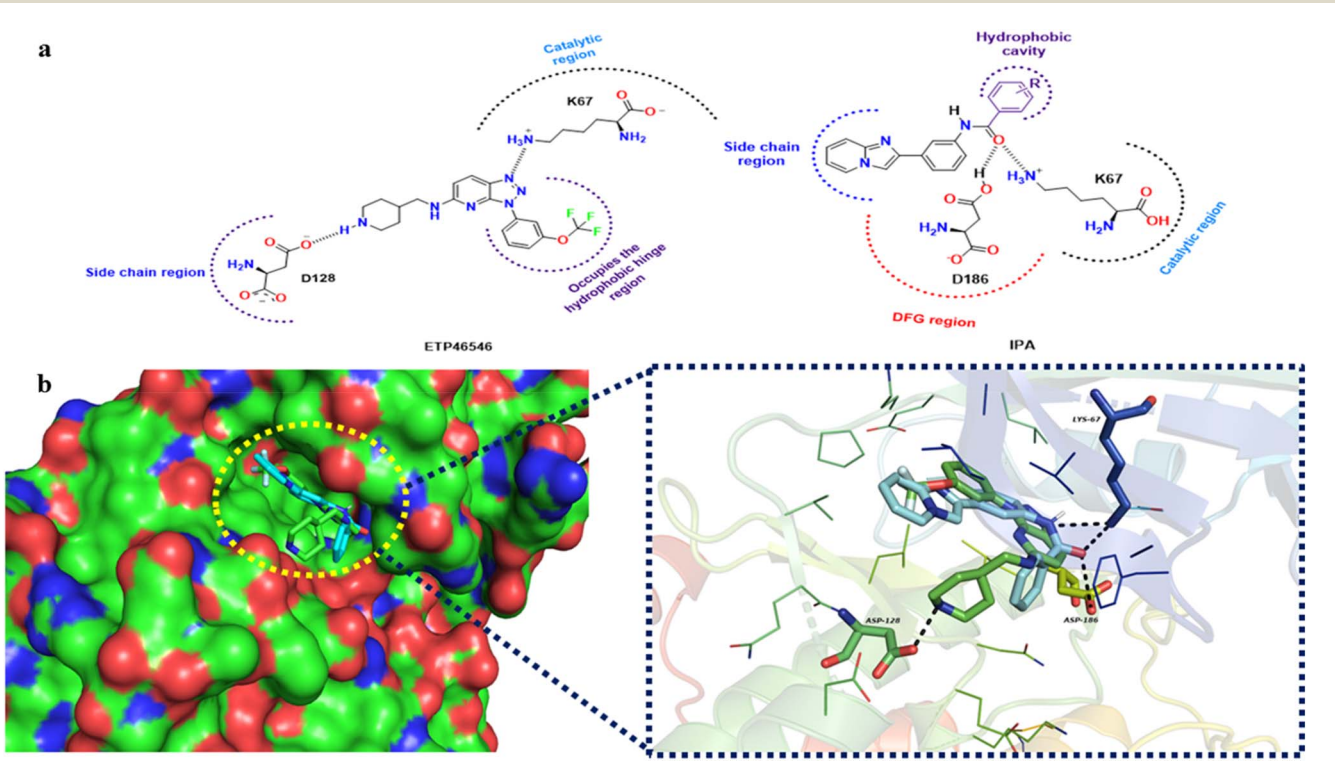

Fig. 3 Molecular docking interactions of PIM-1 kinase inhibitors: (a) ETP46546 facilitated the design of the desired molecule by a structure-scaffold hopping approach and (b) overlap of IPA along with ETP46546 in the binding pocket of PIM-1.

The PIM-1 kinase crystal structure holds a unique active site with Pro123 in the hinge region, which generates a bulge in the binding site and provides a handle for new PIM-1 kinase (Type-2) inhibitor development. Binding site exploration of PIM-1 kinases grounded on molecular docking of PIM-1 kinase inhibiting molecules (LGB321, ETP46546, AZD-1208 and SGI-9481) revealed that the type-II inhibitors interact with the binding area of the receptor, and its active pocket is divided into four regions: hinge, catalytic, DFG motif (hydrogen bond opulent area) and side chain region (hydrophobic area).

3.5. Chemistry

The construction of **3** (2-(3-nitrophenyl)imidazo[1,2-*a*]pyridine) was undertaken by the reaction between 2-amino pyridine **1** and 2-bromo-3′-nitroacetophenone **2** in the presence of $NaHCO_3$ as a base in acetonitrile. Further, **3** was reduced with zinc and HCl, which selectively reduced the primary amine to the amino intermediate **4**. **4** was further derivatized to numerous commensurable amides **6a–r** with substituted benzoyl chlorides **5a–r** in a Schotten–Baumann reaction, and the physical attributes of the target molecules are displayed in Table S1 (SI).

Confirmation of the chemical structure of the synthesized molecules was in concordance with their corresponding FT-IR, ^{1}H and ^{13}C NMR, ESI-MS spectral details. FT-IR evaluation revealed –C═N stretching in the range of 1600–1618 cm^{-1}. The peak at 1640–1678 cm^{-1} was assigned to amide –C═O, 3376–3239 cm^{-1} to amide –NH stretching and 3050–3084 cm^{-1} to aromatic –CH stretching. In the proton NMR analysis, amide –NH protons were identified as singlets at δ values of 10.26–10.69 ppm; aromatic and heteroaromatic hydrogen were observed as multiplets from 8.92–7.37 ppm. The signals of the methyl and methoxy functional-group protons were located at 2.41 and 3.86 ppm as singlets. Moreover, carbon NMR indicated a carbonyl amide signal in the range of 156.76–167.85 ppm and heteroaromatic and aromatic carbon signal at 145.23–109.60 ppm. The entire series of molecules was delineated based on the corresponding molecular ion peaks at the discrete molecular weights.

3.5.1. Scheme of synthesis.

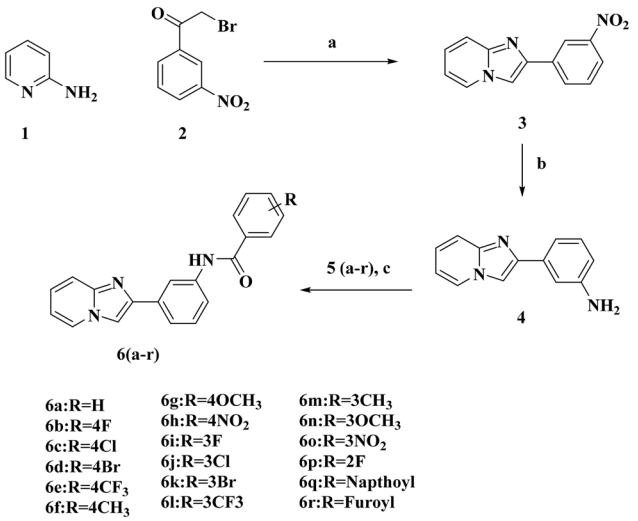

Reagents and conditions: (a) acetonitrile, $NaHCO_3$, stirring at RT for 2 h; (b) Zn, HCl, deionized water, reflux; (c) substituted benzoyl chlorides, DCM, TEA, RT.

3.6. *In vitro* antiproliferative activity

The MTT assay stands is a standard, accurate and appropriate colorimetric method employed for the quantitative assessment of cell proliferation, viability, and activation. Concurrently, PIM kinases have emerged as pivotal players in the realm of tumor cell proliferation. In this context, an investigation into the

Table 3 Antiproliferative activity of compounds **6a–r** for three different cancer cell lines

	PC3	A549	HT29	PCS100–024	SI
Molecule Id	IC_{50} (μM)[b]				
6a	47.92 ± 1.25	25.49 ± 1.59	35.22 ± 1.57	n.d	n.d
6b	29.95 ± 1.5	65.86 ± 3.0	20.34 ± 0.87	57.67 ± 1.62	2.835
6c	44.2 ± 1.56	31.42 ± 1.49	38.1 ± 1.86	n.d	n.d
6d	44.66 ± 2.33	51.87 ± 1.71	41.98 ± 1.74	n.d	n.d
6e	42.48 ± 0.57	46.63 ± 1.1	47.05 ± 0.99	n.d	n.d
6f	**48.45 ± 2.43**	**41.01 ± 1.1**	**39.05 ± 1.27**	**n.d**	**n.d**
6g	40.98 ± 2.27	34.96 ± 2.01	26.17 ± 2.1	n.d	n.d
6h	30.89 ± 1.93	42.02 ± 3.22	18.1 ± 0.44	58.91 ± 2.04	3.254
6i	48.52 ± 1.45	57.38 ± 2.84	42.16 ± 1.09	n.d	n.d
6j	47.33 ± 1.54	57.38 ± 2.84	26.33 ± 1.75	n.d	n.d
6k	38.89 ± 2.11	41.26 ± 1.93	45.3 ± 1.31	n.d	n.d
6l	42.58 ± 1.36	39.88 ± 1.58	34.51 ± 1.62	n.d	n.d
6m	33.73 ± 2.37	40.0 ± 1.9	25.22 ± 0.82	n.d	n.d
6n	44.46 ± 1.65	37.54 ± 1.65	34.13 ± 2.02	n.d	n.d
6o	43.4 ± 2.88	42.76 ± 3.08	31.37 ± 0.55	n.d	n.d
6p	**49.93 ± 1.32**	**37.33 ± 1.02**	**16.41 ± 1.5**	**54.13 ± 1.8**	**3.298**
6q	39.63 ± 3.55	39.77 ± 1.24	32.51 ± 2.53	n.d	n.d
6r	49.33 ± 2.86	42.66 ± 1.67	24.05 ± 1.34	n.d	n.d
5FU[a]	40.86 ± 1.56	42.08 ± 1.1	44.11 ± 1.56	43.53 ± 1.7	0.986

[a] Positive control. [b] IC50 (μM) ± SD of triplicates, $: IC50 of PCS100–024/IC50 of HT29.

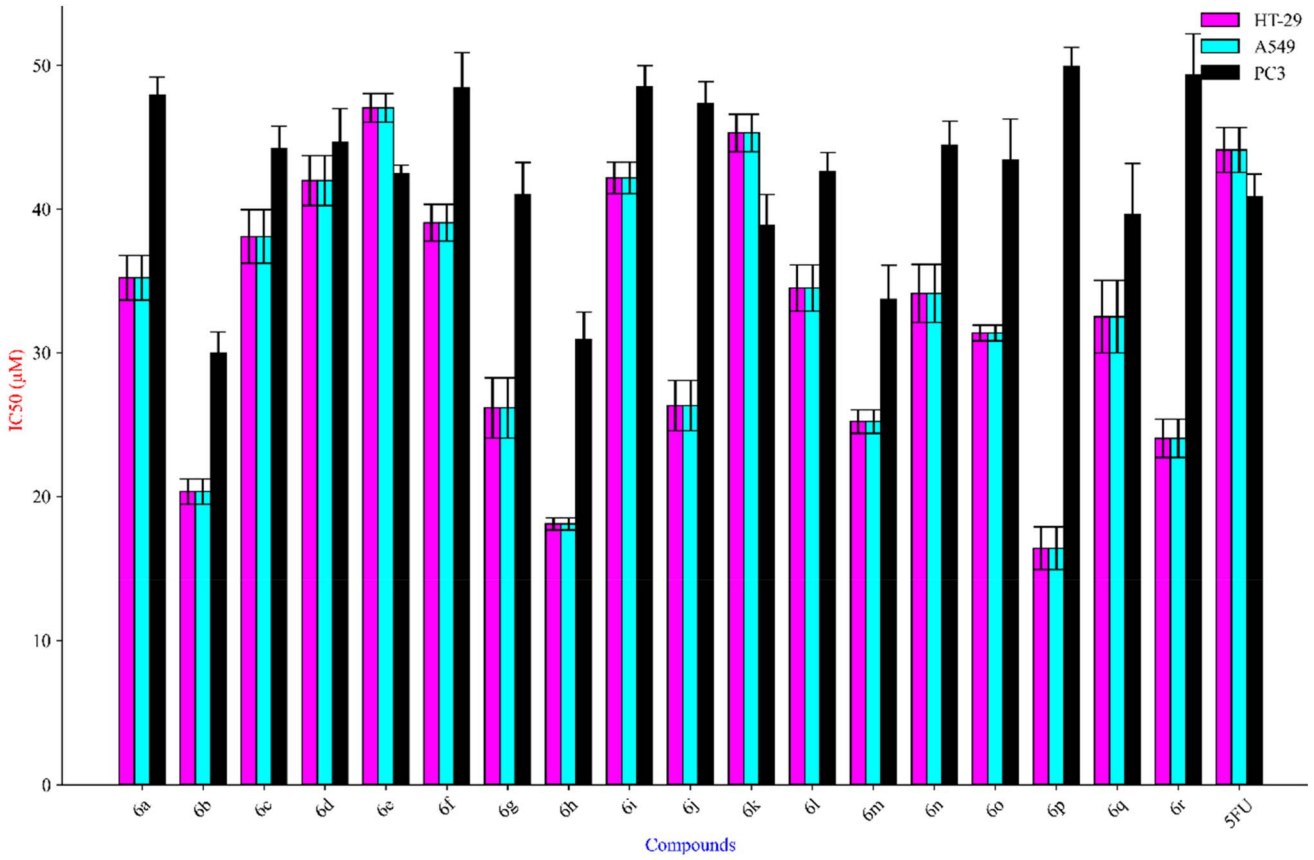

Fig. 4 Graphical illustration of the antiproliferative potential of compounds **6a–r**.

cytotoxicity potential of the synthesized target compounds was undertaken, with the determination of the IC_{50} values across PC3, HT29, and A549 cell lines. Utilizing 5-fluorouracil (**5FU**) as a positive control, the results revealed that the target molecules exhibited notable potency against the PC3 cell line, with IC_{50} values ranging from 29.95 to 49.92 μM, while **5FU** demonstrated comparable potency, possessing an IC_{50} value of 40.96 μM.

Furthermore, the compounds were screened using the HT29 cell line, where they demonstrated varying degrees of activity within the range of 16 to 47 μM. In contrast, **5FU** exhibited potent activity against this cell line, with an IC_{50} value of 43 μM. Similarly, the compounds were evaluated against the A549 cell line, revealing an admirable antiproliferative effect, with IC_{50} ranging from 25.49 to 57.38 μM. Notably, the positive control **5FU**, exhibited an IC_{50} value of 42.08 μM (Table 3).

Among the target analogs, compound **6b** exhibited notable potency, with an IC_{50} value of 29.25 μM, showcasing encouraging efficacy against the PC3 cell line. Conversely, compounds **6p** (49.92 μM) and **6r** (49.32 μM) demonstrated comparatively lower potency against PC3, in contrast to the positive control **5FU**, which exhibited an IC_{50} value of 40.96 μM. Intriguingly, compounds **6p** (18 μM) and **6h** (16 μM) displayed excellent potential in inhibiting HT29 cell proliferation. On the other hand, compounds **6d** (42 μM) **6e** (74 μM), **6i** (42 μM) and **6k** (45 μM) exhibited lower activity against the HT29 cell line compared to **5FU** (43 μM).

Besides, in the case of the A549 cell line, compounds **6a** (25.49 μM) and **6c** (31.41 μM) demonstrated improved activity over **5FU** (42.08 μM). This underscores the promising antiproliferative effects of these specific analogs across different cell lines. The results suggest a nuanced spectrum of potency among the synthesized compounds, emphasizing their potential as candidates for further investigation and development in the context of cancer cell proliferation inhibition (Fig. 4).

In continuation of antiproliferative studies on three cancerous cell lines, three compounds **6b**, **6h** and **6p**, along with the standard 5-fluorouracil, were screened against the normal cell line PCS1000-024 in order to explore the selectivity index. The three tested molecules demonstrated IC_{50} values of 57.67, 58.91 and 54.13 μM, compared to 43.53 μM for 5FU.[31] All three exhibited greater IC_{50} in comparison to 5FU. The selectivity index is the ratio of IC_{50} for the normal cell line *versus* that of the HT29 cell line, and a SI value greater than 2.0 is essentially a favorable value. The SI values calculated for the three tested molecules were found to be 2.835, 3.254 and 3.298, which are favorable values, while 5FU showed the calculated SI value of 0.986.

3.7. *In vitro* PIM-1 kinase inhibitory activity

The PIM-1 kinase inhibitory assay is based on chemiluminescence, which was found to be the most precise method for evaluation. Herein, an evaluation of the enzyme inhibitory

Table 4 PIM-1 kinase inhibitory activity of compounds **6a–r**

Molecule Id	PIM-1 kinase % inhibition at 10 μM
6a	11.6 ± 2.1
6b	13.0 ± 2.4
6c	17.0 ± 1.9
6d	14.1 ± 0.3
6e	13.0 ± 1.3
6f	9.8 ± 1.1
6g	22.1 ± 2.8
6h	**34.5 ± 3.4**
6i	**32.7 ± 2.5**
6j	10.0 ± 1.9
6k	22.9 ± 1.0
6l	21.9 ± 1.1
6m	25.4 ± 2.6
6n	26.5 ± 2.7
6o	26.8 ± 2.1
6p	**28.0 ± 2.3**
6q	19.6 ± 1.0
6r	18.2 ± 2.4
Staurosporine	70.2 ± 1.1

potential against PIM-1 kinase for the target molecules was performed to determine the % inhibition at a concentration of 10 μM by employing staurosporine as a standard drug. The results demonstrated inhibition of PIM-1 in the range of 9.8% ± 1.1% to 34.5% ± 3.4%, compared with the standard staurosporine (70.2% ± 1.1%).

Furthermore, the synthesized compounds **6h** and **6i** demonstrated excellent inhibitory activity of 34.5% ± 3.4% and 32.7% ± 2.5%. Molecules **6k** to **6p** were spotted as moderately active, with % inhibitory potentials in the range of 22.9% ± 1.0% to 28.0% ± 2.3%, where **6n** and **6o** revealed a similar inhibitory activity of 26.5% ± 2.7% and 26.8% ± 2.1% with a minimal SE.

Compound **6f** was noted with the lowest inhibitory effect of 9.8% ± 1.1% from the series of synthesized compounds, as compared to the positive control with a corresponding % inhibition of 70.2% ± 1.1%, as depicted in Table 4.

3.8. Apoptosis induction in HT-29 cells

Apoptosis is a regulated form of planned cell death that plays an indispensable role in normal development and tissue homeostasis. Any aberration in this process eventually leads to various pathological conditions, including Alzheimer's disease and malignancies like cancer. Apoptosis is characterized by distinct morphological and biochemical changes, in contrast to necrosis, which is a form of accidental cell death. Key features of apoptosis include chromatin condensation and fragmentation, cytoplasm shrinkage, and alterations in membrane asymmetry. These changes collectively facilitate the orderly dismantling and removal of cells without eliciting an inflammatory response.

In order to study whether tumour cells treated with the control and target compounds show apoptosis, HT-29 cells were smeared using Annexin V and PI. FACS (Fluorescence Assisted Cell Sorting) can separate cells into four parts *viz.*, Annexin V– PI- (live cells); Annexin V + PI- (early apoptotic cells); Annexin V + PI+ (late apoptotic cells) and Annexin V– PI + (necrotic cell). To

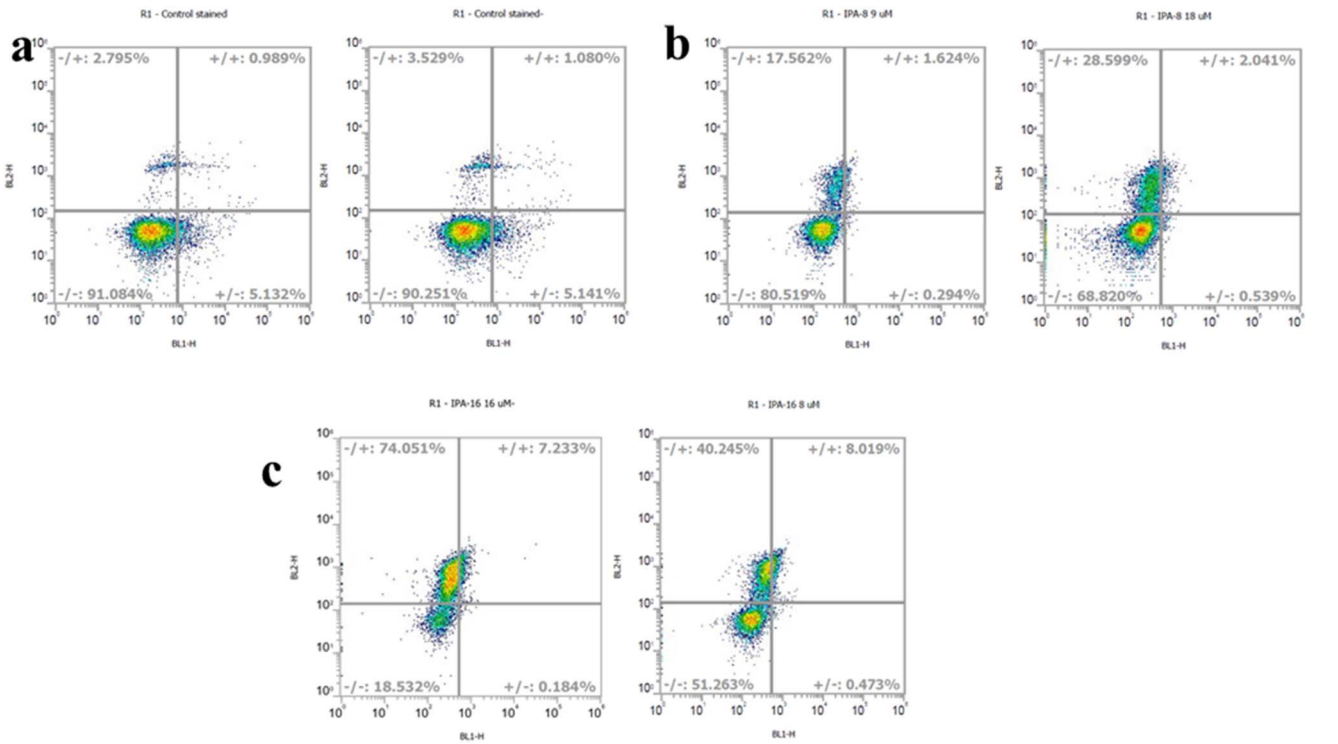

Fig. 5 Flow cytometry analysis of **6h** and **6p** for the determination of apoptosis in the HT-29 cell line, analysis from FACS with Annexin V *vs.* PI on HT-29 (a) control, (b) **6h** and (c) **6p**.

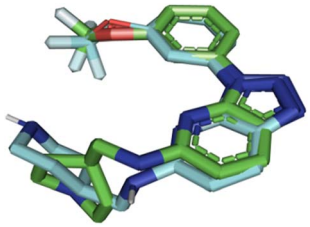

Fig. 6 Conformational pose of the docked geometry (cyan) and co-crystal ligand (green).

evaluate the antiproliferative effects of the compounds on the HT-29 cell line, **6h** and **6p** were selected for the assay. **6h** and **6p** demonstrated IC_{50} of 9 and 16 μM, respectively, resulting in a high count of necrotic cells (28.59, 74.05%) compared to the untreated cells (<1%). Upon treatment with **6p**, 74.05% necrotic cells and 7.23% late apoptotic cells were identified, indicating that **6p** induces apoptosis of HT-29 cells, as illustrated in Fig. 5.

3.9. Molecular docking analysis of target compounds

Molecular docking analysis was explored to identify the binding mode of the designed kinase inhibitors to the active site of PIM-1 kinase. To validate the docking protocol, the co-crystal ligand

Table 5 Molecular contacts and docking score of compounds

Comp. no.	Docking energy (kcal mol^{-1})	Hydrogen bond contacts	Electrostatic and hydrophobic interactions
ETP46546 (Co-crystal ligand)	−8.9	Lys67 and Asp128	Leu44, Val52, Phe49, Ala65, Ile104, Val126, Leu120, Glu171, and Ile185
6a	−9.8	Lys67 and Asp186	Leu44, Phe49, Val52, Ala65, Ile104, Leu120, Val126, Leu174 and Ile185
6b	−10.0	Lys67 and Asp186	Leu44, Val52, Phe49, Ala65, Ile104, Val126, Leu120, Glu171, and Ile185
6c		Lys67 and Asp186	Leu44, Val52, Phe49, Ala65, Ile104, Val126, Leu120, Glu171, and Ile185
6d	−10.1	Lys67 and Asp186	Leu44, Phe49, Val52, Ala65, Ile104, Leu120, Val126, Glu171, and Ile185
6e	−10.4	Lys67 and Asp186	Leu44, Val52, Phe49, Ala65, Ile104, Val126, Leu120, Glu171, Ile185, Val126, Asp128, Glu171, Leu174 and Ile185
6f	−10.2	Lys67 and Asp186	Leu44, Val52, Phe49, Ala65, Ile104, Val126, Leu120, Glu171, and Ile185
6g	−9.8	Lys67 and Asp186	Leu44, Val52, Phe49, Ala65, Ile104, Leu120, Arg122, Val126, Glu171, Asn172, Leu174 and Ile185
6h	−10.0	Lys67, Glu171 and Asp186	Leu44, Val52, Phe49, Ala65, Ile104, Leu120, Val126, Glu171, and Ile185
6i	−10.1	Lys67 and Asp186	Leu44, Gly45, Phe49, Val52, Ala65, Leu120, Ile104, Arg122, Val126, Asn172, Glu171, Leu174 and Ile185
6j		Lys67 and Asp186	Leu44, Gly45, Phe49, Val52, Ala65, Ile104, Leu120, Arg122, Val126, Glu171, Asn172, Leu174 and Ile185
6k	−10.2	Lys67 and Asp186	Leu44, Gly45, Phe49, Val52, Ala65, Ile104, Leu120, Val126, Leu174 and Ile185
6l	−10.6	Lys67 and Asp186	Leu44, Val52, Phe49, Ala65, Ile104, Leu120, Val126, Leu174 and Ile185
6m	−10.5	Lys67 and Asp186	Leu44, Val52, Phe49, Ala65, Ile104, Leu120, Val126, Leu174 and Ile185
6n	−10.0	Lys67 and Asp186	Leu44, Val52, Phe49, Ala65, Ile104, Leu120, Val126, Glu171, Leu174 and Ile185
6o	−9.7	Lys67,Glu171, Asn172and Asp186	Leu44, Val52, Phe49, Ala65, Ile104, Leu120, Val126, Glu171, Leu174 and Ile185
6p	−9.8	Lys67 and Asp186	Leu44, Val52, Phe49, Ala65, Ile104, Leu120, Val126, Glu171, Leu174 and Ile185
6r	−9.1	Lys67 and Asp186	Leu44, Val52, Phe49, Ala65, Ile104, Leu120, Val126, Glu171, Leu174 and Ile185

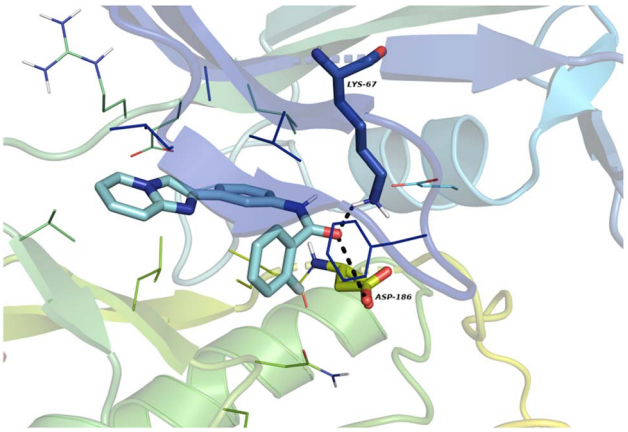

Fig. 7 Docked complex of **6p** with PIM-1 kinase.

(ETP46546) was re-docked, and both the docked conformation and crystal ligand conformation were aligned, which displayed RMSD = 0.25 Å, as depicted in Fig. 6. All the tested compounds were docked in the active site of the PIM-1 kinase, and their corresponding docking scores are summarized in Table 5.

The most potent molecule **6p**, with an IC_{50} value of 16 μM for HT29, docked in the binding pocket of PIM-1 kinase, with docking energy = −9.8 kcal mol^{-1}. The amide functional group formed polar hydrogen bonds with Lys67 (2.1 Å) and Asp186 (2 Å) in the catalytic region and with the DFG motif. The spacer phenyl ring established π-sigma interaction with Ile185 (3.9 Å). Moreover, the 2-fluoro phenyl ring generated π–π stacking hydrophobic interactions with Phe49 (4 Å) in the side pocket. In the lipophilic groove, the imidazopyridine ring was surrounded by Leu44 (3.90 Å), Ala65 (4.9 Å), Val126 (4.7 Å) and Leu174 (4.9 Å) and established π-alkyl contacts, as depicted in Fig. 7.

The active compound **6a** with an IC_{50} value of 25.49 μM for A549 resided in the active pocket of the protein, with a docking energy of −9.8 kcal mol^{-1}. The carbonyl amide functionality generated hydrogen bond contacts with Lys67 (2.09 Å) and Asp186 (2.2 Å) in the catalytic and DFG motifs. The imidazopyridine and the central phenyl ring resided in the hydrophobic pocket, surrounded by amino acids, namely, Leu44 (3.90, 4.88 Å), Ala65 (5.1, 4.8 Å), Val126 (4.7 Å) and Leu174 (4.9 Å), and established π-alkyl contacts. The phenyl ring of the amide group generated π–π stacking with Phe49 (4.1 Å), as shown in Fig. 8.

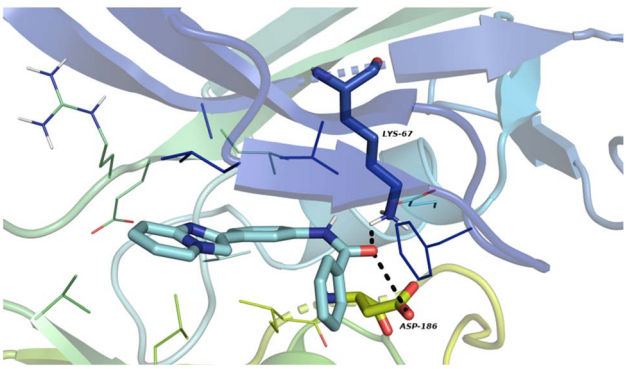

Fig. 8 Docked complex of **6a** with PIM-1 kinase.

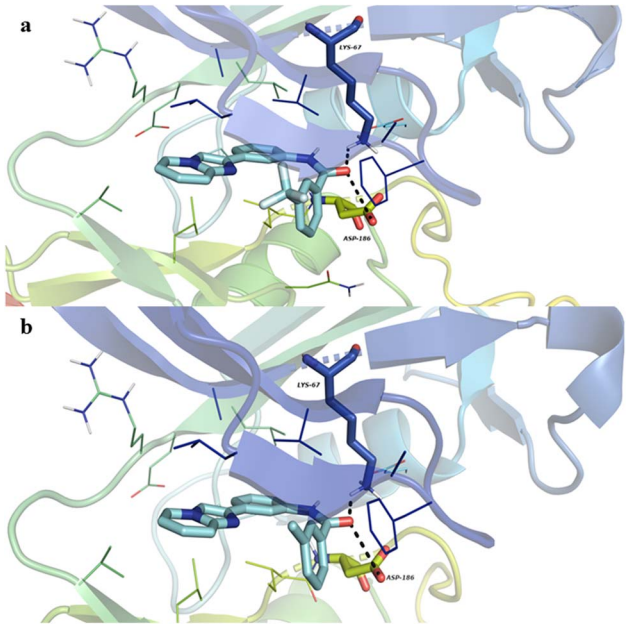

Fig. 9 Docked complex of PIM-1 kinase with (a) **6l** and (b) **6m**.

Compounds **6l** and **6m**, with docking energies of −10.6 and −10.5 kcal mol^{-1}, respectively, well occupied the active cavity of PIM-1 kinase. The carbonyl oxygen of the amide functionality (**6l** and **6m**) established two hydrogen bond interactions with the hydrogen on the terminal nitrogen of Lys67 (2.1 Å) and Asp186 (2.2 Å) in the catalytic region and DFG motif. The imidazopyridine and central phenyl rings were precisely placed in the hydrophobic cavity, forming hydrophobic π-alkyl contacts with Leu44 (4.91 Å), Val126 (4.7 Å) and Leu174 (5.9 Å), as well as electrostatic π-sigma interactions with Ile185 (5.16 Å). The 3-trifluoromethylphenyl and 3-methylphenyl moieties generated π–π stacking and π-alkyl interactions with Phe47 (5.8 Å) in the corner hydrophobic region of the kinase, as shown in Fig. 9.

Molecule **6e** was perfectly positioned in the active-site pocket of PIM-1 kinase; the oxygen of the amide carbonyl formed two polar hydrogen bond interactions with Lys67 (2.1 Å) in the catalytic groove and Asp186 (2.9 Å) in the DFG motif. The

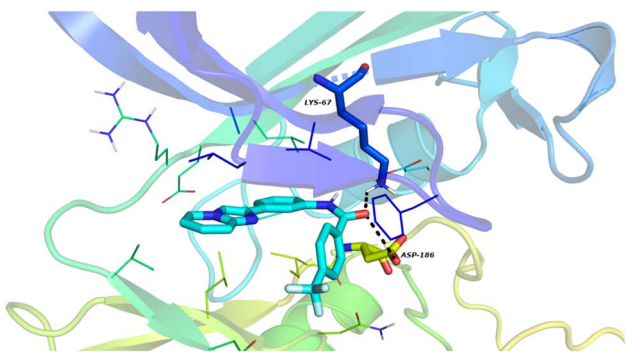

Fig. 10 Docked complex of **6e** with PIM-1 kinase.

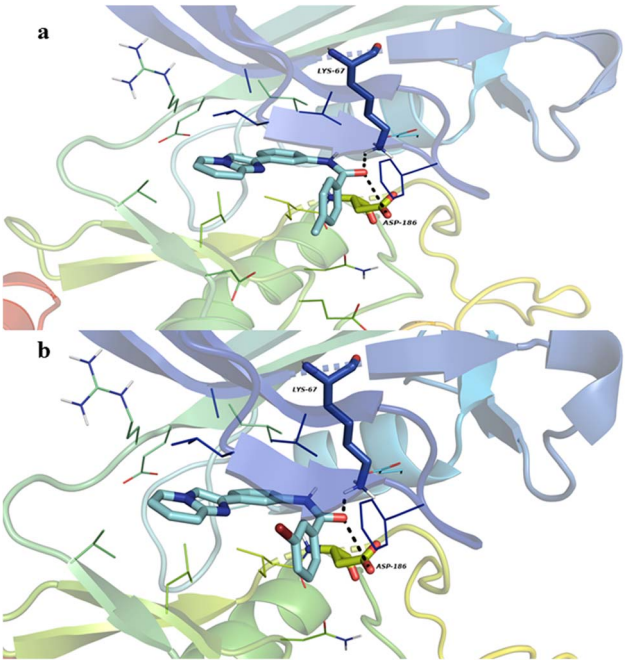

Fig. 11 Docked complex of PIM-1 kinase with (a) **6f** and (b) **6k**.

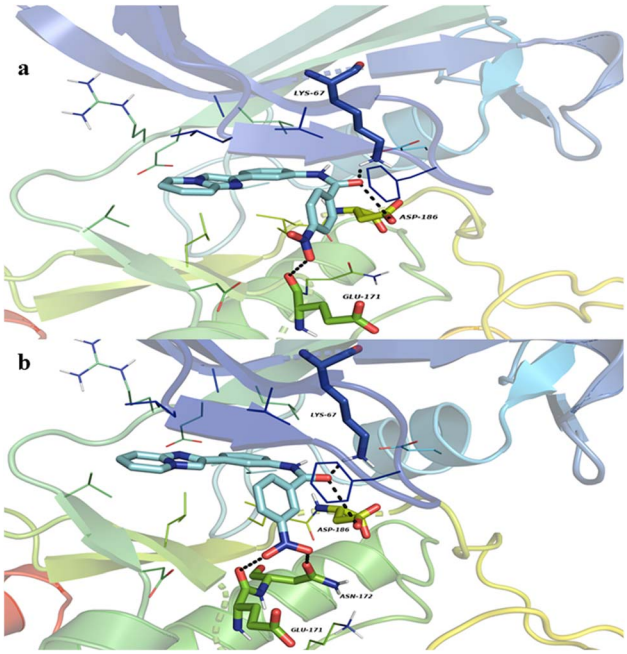

Fig. 12 Docked complex of PIM-1 kinase with (a) **6h** and (b) **6o**.

imidazopyridine and central phenyl ring occupied the hydrophobic region of the protein, and the imidazopyridine fragment generated π-alkyl contacts with Leu44 (4.84, 4.87 Å), Val52 (6.77 Å), Val126 (4.72 Å) and Leu174 (5.99 Å). Moreover, the phenyl ring connected to the imidazopyridine nucleus established π-sigma and π-alkyl interactions with Ala65, Leu120, and Ile185. The trifluoromethyphenyl flanked with amide functional groups established π-sigma and π–π stacking contacts with Ile185 and Phe49 in the side hydrophobic pocket, with a corresponding docking energy of −10.4 kcal mol^{-1}, as depicted in Fig. 10.

Molecules **6f** and **6k** were properly positioned in the binding area of PIM-1 kinase, with a docking energy of −10.2 kcal mol^{-1}. The amide functionality of both compounds established hydrogen bond contacts with Lys67 (2.08, 2.10 Å) and Asp186 (3.2 Å) in the catalytic and DFG motifs. The imidazopyridine fragment of both compounds, located in the hydrophobic pocket, formed π-alkyl contacts with Leu44 (4.87 Å), Val52 (5.50 Å), Ala65 (5.20, 4.80 Å), Ile104 (5.38, 5.50 Å), Leu120 (5.11 Å), and Val126(5.23, 4.88 Å), as well as π-sigma interactions with Ile185(3.9 Å). Similar interactions were noticed for the central phenyl ring attached to the imidazoypridine. The 3-Br and 4-CH_3 phenyl moieties established π–π stacking interactions with Phe49 (4.05, 4.09 Å) in the side hydrophobic cavity, as depicted in Fig. 11.

Compounds **6h** and **6o** having a –NO_2 functionality at the *para* and *meta* positions are the isomeric forms of each other and reside in the active pocket of PIM-1 kinase, with corresponding docking energies of −10.0 and −9.7 kcal mol^{-1}. Imidazoypridine and the spacer phenyl ring of the isomers developed electrostatic π-sigma interactions with Leu44 (3.98 Å) and Ile185 (3.92, 3.96 Å) but the 4-NO_2 phenyl ring also established an additional π-sigma contact with Ile185 (3.99 Å) and π–π stacking interaction with Phe49 (3.98, 4.10 Å) in the corner side hydrophobic cavity. The amide functionality of the isomers formed polar hydrogen bond contacts with Lys67 (2.09 Å) and Asp186 (3.4 Å). Moreover, the –NO_2functional group generated three polar hydrogen bond contacts with Glu171 (3.4 Å) and Asn172 (3.1 Å) in the side-chain region, as shown in Fig. 12.

3.9.1. MD simulation analysis. On the basis of the cell proliferation and molecular docking simulation studies, compound **6h** formed the anticipated molecular contacts within the active site, and was further selected for molecular dynamics simulation to ascertain the residential stability throughout 100 ns of MD simulation. The complex was examined based on the root mean square deviation (RMSD), radius of gyration (Rg), root mean square fluctuation (RMSF) and hydrogen bond formation.

3.9.2 RMSD plot. At the initial stage of MD, protein (4A7C) RMSD was observed from 1.5 Å, with a continuous rise in the spikes up to 2.25 Å until 10 ns. Followed by this phase, the RMSD became stable at around 2 Å; further, a sudden spike in the fluctuations was spotted nearing 3 Å at 25 to 30 ns. Followed by this raised spike, a gradual decrease in the RMSD reaching 2 Å, followed by a constant RMSD, was observed up to 70 ns. At 75 ns, a marginal dip was observed in the RMSD, which further spiked to 2.25 Å. This continued for a few ns, and finally, the protein reached equilibrium at 2 Å towards the end of the MD timeframe (Fig. 13a).

The RMSD of macromolecule ligand (**6h**) was also analysed, indicating that in the inceptive phase, RMSD spikes were noticed from 3 and increased to 6 Å at 5 ns. A sudden downfall in the projections was observed at 2–3 Å in the timeframe of 6 to

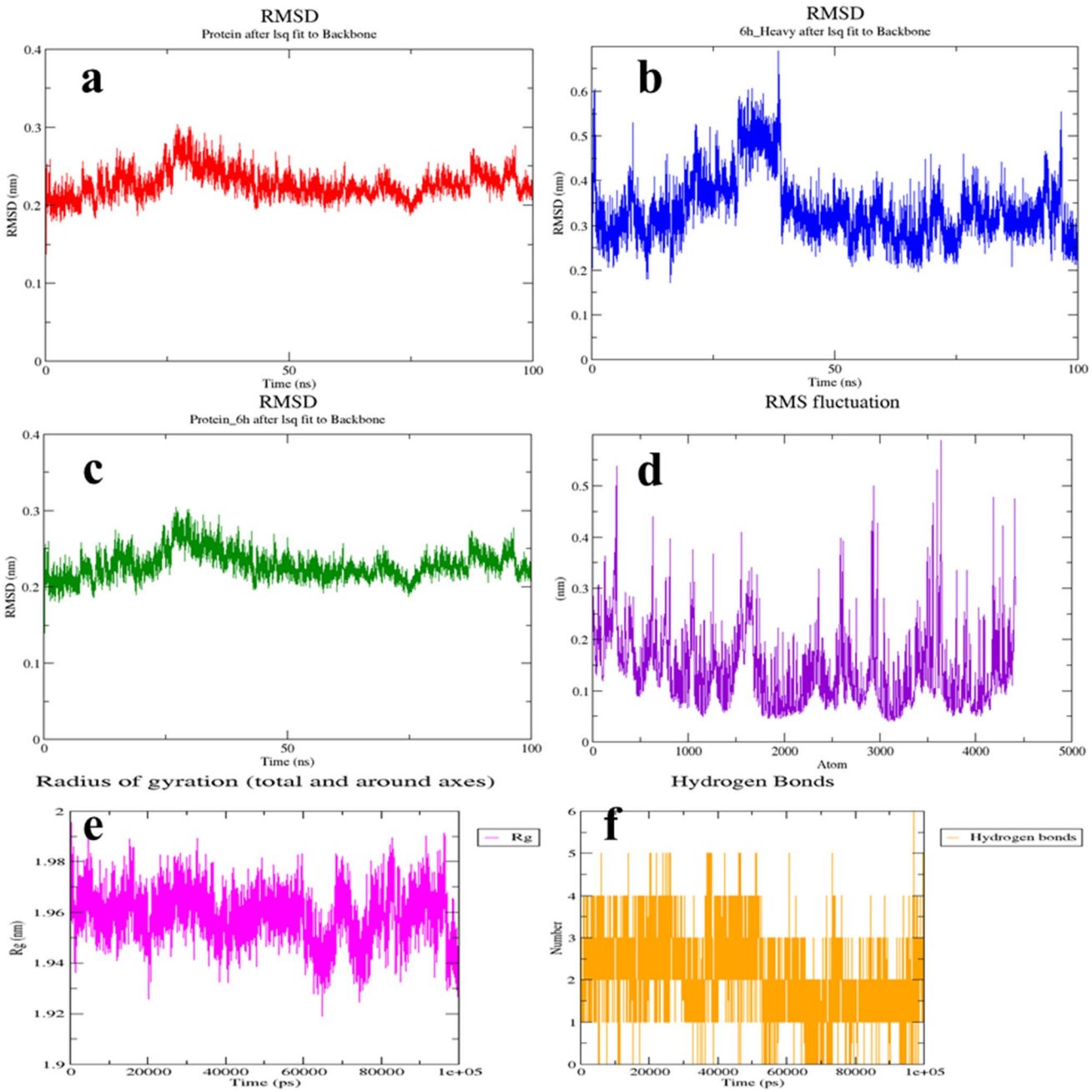

Fig. 13 (a–c) RMSD graphical representations of PIM-1 kinase, **6h** and the protein-**6h** complex; (d) RMSF plot; (e) Rg graph; and (f) hydrogen bond plot.

25 ns; furthermore, a tangential increase in the RMSD at 3.5–4 Å was observed at 30 ns, indicating a moderate conformational change in **6h**. From 35 to 45 ns, a sudden rise in the ligand RMSD projections to 6 Å was observed, followed by a quick downfall to 3 Å. From 46–100 ns, the ligand obtained conformational stability, with a continuous rise and fall in the RMSD spikes at 2.5–3 Å, as illustrated in Fig. 13b.

Evaluation of the 4A7C-6h complex showed an encouraging stability profile throughout the MD simulation, with RMSDs ranging from 2 to 2.5 Å, with minimal alterations in the RMSD projections. It was noticed that the nascent ligand displayed average stability features as compared to the ligand protein complex (Fig. 13c).

3.9.3 RMSF graph. RMSF indicates the divergence of the average coordinates of the amino acids from the initial points during the simulation trajectory. In the graphical representation, the RMSF contour of the protein is depicted in azure. From previously observed, the terminal amino acid residues showed larger fluctuations, which are not the part of the binding site, as depicted in Fig. 13d.[31]

3.9.4 Rg plot. Rg reflects the compactness of the protein-ligand complex during the entire MD trajectory period. Rg

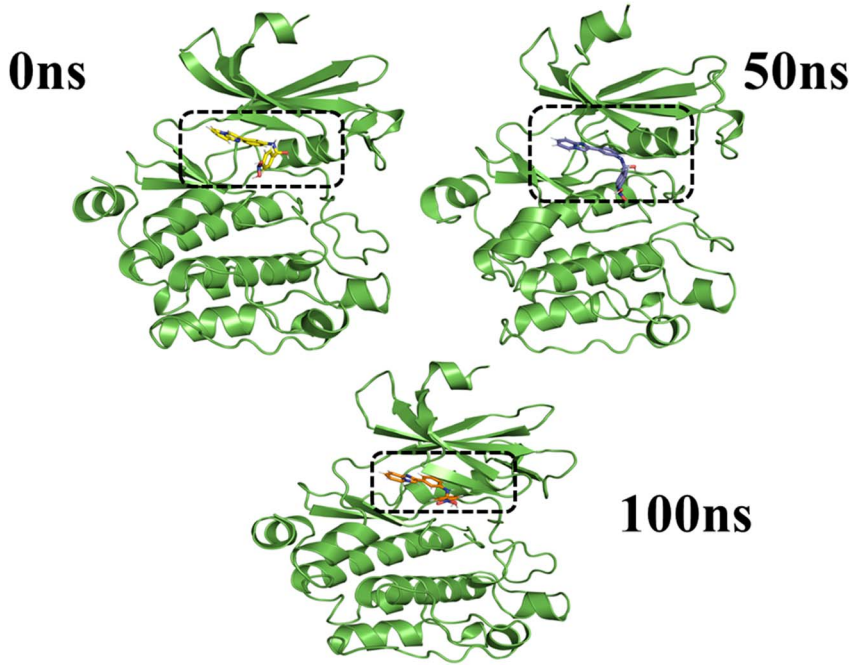

Fig. 14 Conformational patterns of the PIM-1 kinase-**6h** complex at three different MD timeframes.

spikes were observed at 1.95 Å at the onset of MD, increased to 1.98 Å between 1-17 ns, and at 20 ns, a fall in the RG spikes was observed. Onwards, an equilibrium phase with a maximum of 1.98 Å in the Rg fluctuations was observed up to 40 ns, with an average of 1.95 Å. The same kind of pattern was noticed with an Rg peak of 1.93 Å at 65 ns. From 70 ns till the end of the MD simulation phase, a pattern of rise and dips was observed, peaking at 1.99 Å, and at 100 ns, it was stabilized at 1.93 Å, as depicted in the Fig. 13e.

3.9.5 Hydrogen bonding analysis. Protein–ligand interactions are indispensable for the proper conformation, and are explained by MD trajectories. Among such interactions, hydrogen bonding interactions stand at the forefront, indicating stability of the ligand in the binding pocket of the protein. Trajectory analysis revealed that **6h** established a maximum of four hydrogen-bond interactions with the protein over the duration of the MD trajectory (Fig. 13f and 14).

3.10. *In silico* ADME and drug-likeliness prediction

All the synthesized compounds were subjected to ADMET profiling and drug-likeness assessment employing the free online software https://.www.swissadme.ch/index.php and

Table 6 Analysis of computed ADMET profiles and drug-likeliness of the compounds

Molecule Id	MW	TPSA (Å^2)	Log *P*	HA	HD	Rotatable bonds	Lipinski rule	% Abs	Log BB	CLtot (log ml min^{-1} kg^{-1})	Hepatotoxicity
6a	313.35	46.4	4.25	2	1	4	Yes	92.92	0.48	0.73	No
6b	331.34	46.4	4.39	3	1	4		92.58	0.46	0.69	Yes
6c	347.8	46.4	4.90	2	1	4		91.52	0.46	0.72	No
6d	392.25	46.4	5.01	2	1	4		91.46	0.45	0.71	
6e	381.35	46.4	5.27	5	1	4		90.60	0.46	0.59	
6f	327.38	46.4	4.56	2	1	4		92.98	0.47	0.74	
6g	343.38	55.6	4.26	3	1	5		94.03	0.33	0.76	Yes
6h	358.35	92.2	4.16	4	1	5		91.15	−0.69	0.50	No
6i	331.34	46.4	4.39	3	1	4		93.06	0.45	0.65	Yes
6j	347.8	46.4	4.90	2	1	4		91.95	0.45	0.66	No
6k	392.25	46.4	5.01	2	1	4		91.88	0.45	0.61	
6l	381.35	46.4	5.27	5	1	5		91.02	0.45	0.54	
6m	327.38	46.4	4.56	2	1	4		93.40	0.47	0.71	
6n	343.38	55.6	4.26	3	1	5		94.51	0.32	0.72	Yes
6o	358.35	92.2	4.16	4	1	5		91.93	−0.68	0.46	No
6p	331.34	46.4	4.39	3	1	4		92.38	0.49	0.64	
6q	363.41	46.4	5.40	2	1	4		93.32	0.5	0.72	
6r	303.31	59.5	3.84	3	1	4		92.96	0.44	0.79	

https://.biosig.unimelb.edu.au/pkcsm. All the screened molecules were tested for the *in silico* ADMET features by using SwissADME. The molecular weight calculated for all the molecules was in the range of 303.31–392.25 Da, with a maximum count of 5 HBA and 1 HBD. The TPSA of the compounds under scrutiny, **6a–f**, **6i–m**, **6q**, were calculated with TPSA of 46.4 Å^2 while **6g**, **6n**, showed 55.63 Å^2 with **6r**, was 59.54 Å^2 and for **6h**, and **6o**, it was 92.22 Å^2 demonstrated values of 46.4, 55.63, 59.54 and 92.22 Å^2, respectively, with log *P* values ranging from 3.84 to 5.40. All molecules fall in the window of Lipinski's rule of 5 (Lipinski RO5) without any violation.

Moreover, the compounds were predicted to have excellent intestinal absorption, from which the potent molecules **6a**, **6b**, **6c**, **6h** and **6p** exhibited % absorptions of 92.92, 92.58, 91.52, 91.15 and 92.38%, respectively. The potent compounds are more readily transported through the BBB, among which **6h** demonstrated poor distribution through the BBB. The most active compounds **6a**, **6c**, **6h**, and **6p** were safe and did not induce hepatotoxicity, whereas **6b** induced hepatotoxicity. Overall, the synthesized molecules were drug-like according to the LRO5, and displayed excellent ADMET profiles. The detailed analysis is presented in Table 6.

4. Conclusion

In conclusion, this research article revealed the comprehensive utility of various computation and machine learning tools in designing new compounds with different scaffolds for PIM1 inhibitory activity. The designed molecules were synthesized, characterized and subjected to numerous *in vitro* evaluations, including PIM1 inhibitory assay at 10 μM concentration. Among the synthesized compounds, **6h** displayed superior antiproliferative activity against colon cancer cell lines, with an IC_{50} of 18.1 ± 0.44 μM. **6h** could prompt apoptosis and prevent the growth of HT-29 cells due to its antiproliferative potential, thus augmenting its therapeutic potential against cancer cells. In order to confirm our hypothesis of PIM1 kinase inhibition, all compounds were tested at a fixed concentration for kinase inhibitory activity, which revealed moderate kinase inhibitory potentials of 34.5% ± 3.4%. Further, structure-based computational studies, including docking and molecular dynamics simulation, strengthened the approach, with favorable ADMET property predictions. Further, *in vivo* evaluation coupled with determination of the kinase inhibitory IC_{50} values confirmed the computational and machine learning approach for medicinal chemistry.

Ethical statement

This research has been protected by filing a Patent (Indian Patent Application No. IN202421052696, 2024).

Author contributions

All the authors contributed equally and approved the final version of the manuscript.

Conflicts of interest

The authors declare no financial interest that could appear to affect the research work.

Data availability

The data used for development of the ML models were obtained from open source published research articles. The codes for the ML were composed in-house on Jupiter note book and have not been taken from any other sources. The molecular docking results are included in the manuscript. The molecular dynamics simulation output files are very large in size and hence cannot be shared. The data derived from MDS such as RMSD, RG, RMSF and HB are included in the document.

Supplementary information (SI) is available. See DOI: https://doi.org/10.1039/d6ra00514d.

Acknowledgements

VW extends gratitude to the Principal, Poona College of Pharmacy, Pune, for the constant encouragement. RK thanks the Management team of BLDEA University for providing the necessary help in cell line studies.

References

1 A. Upadhyay, Cancer: An unknown territory; rethinking before going ahead, *Gene. Dis.*, 2021, **8**, 655–661, DOI: 10.1016/j.gendis.2020.09.002.
2 S. Pandiyan and L. Wang, A comprehensive review on recent approaches for cancer drug discovery associated with artificial intelligence, *Comput. Biol. Med.*, 2022, **150**, 106140, DOI: 10.1016/j.compbiomed.2022.106140.
3 K. S. Bhullar, N. O. Lagarón, E. M. McGowan, I. Parmar, A. Jha, B. P. Hubbard and H. P. V. Rupasinghe, Kinase-targeted cancer therapies: progress, challenges and future directions, *Mol. Cancer*, 2018, **17**, 1–20, DOI: 10.1186/s12943-018-0804-2.
4 A. Turdo, C. D'Accardo, A. Glaviano, G. Porcelli, C. Colarossi, L. Colarossi, M. Mare, N. Faldetta, C. Modica, G. Pistone, M. R. Bongiorno, M. Todaro and G. Stassi, Targeting phosphatases and kinases: how to checkmate cancer, *Front. Cell Dev. Biol.*, 2021, **9**, 690306, DOI: 10.3389/fcell.2021.690306.
5 R. R. Naik and A. K. Shakya, Exploring the chemotherapeutic potential of currently used kinase inhibitors: An update, *Front. Pharmacol*, 2023, **13**, 1064472, DOI: 10.3389/fphar.2022.1064472.
6 M. Bellon and C. Nicot, Targeting Pim kinases in hematological cancers: molecular and clinical review, *Mol. Cancer*, 2023, **22**, 18, DOI: 10.1186/s12943-023-01721-1.
7 S. Nandi, M. Salman, A. Sharma and M. Kumar, Signal transduction through JAK-STAT and NF-κB regulated Pim-1 Kinase: Novel target for anticancer leads, *Curr. Signal Transduct. Ther.*, 2018, **13**, 83–104, DOI: 10.2174/1574888X13666180301124935.

8 M. Bachmann, H. Hennemann, P. X. Xing, I. Hoffmann and T. Möröy, The Oncogenic Serine/Threonine Kinase Pim-1 phosphorylates and inhibits the activity of Cdc25C-associated kinase 1 (C-TAK1), *J. Biol. Chem.*, 2004, **279**, 48319–48328, DOI: 10.1074/jbc.M404440200.

9 Y. Peng, J. Li, F. Xie, J. Chen, Y. Yu, X. Ouyang and H. Liang, expression of pim-1 in tumors, tumor stroma and tumor-adjacent mucosa co-determines the prognosis of colon cancer patients, *PLoS One*, 2013, **8**, e76693, DOI: 10.1371/journal.pone.0076693.

10 M. Zhang, T. Liu, H. Sun, W. Weng, Q. Zhang, C. Liu, Y. Han and W. Sheng, Pim1 supports human colorectal cancer growth during glucose deprivation by enhancing the Warburg effect, *Cancer Sci.*, 2018, **109**, 1468–1479, DOI: 10.1111/cas.13562.

11 S. S. Chauhan, R. K. Toth, C. C. Jensen, A. L. Casillas, D. F. Kashatus and N. A. Warfel, PIM kinases alter mitochondrial dynamics and chemosensitivity in lung cancer, *Oncogene*, 2020, **39**, 2597–2611, DOI: 10.1038/s41388-020-1168-9.

12 J. H. Song and A. S. Kraft, Pim kinase inhibitors sensitize prostate cancer cells to apoptosis triggered by Bcl-2 family inhibitor ABT-737, *Cancer Res.*, 2012, **72**, 294–303, DOI: 10.1158/0008-5472.CAN-11-3240.

13 C. Blanco-Aparicio and A. Carnero, Pim kinases in cancer: Diagnostic, prognostic and treatment opportunities, *Biochem. Pharmacol.*, 2013, **85**, 629–643, DOI: 10.1016/j.bcp.2012.09.018.

14 X. Tang, T. Cao, Y. Zhu, L. Zhang, J. Chen, T. Liu, X. Ming, S. Fang, Y. Yuan, L. Jiang, J.-D. Huang and X.-Y. Guan, PIM2 promotes hepatocellular carcinoma tumorigenesis and progression through activating NF-κB signaling pathway, *Cell Death Dis.*, 2020, **11**, 510, DOI: 10.1038/s41419-020-2700-0.

15 V. Walhekar, C. Bagul, D. Kumar, A. Muthal, G. Achaiah and R. Kulkarni, Topical advances in PIM kinases and their inhibitors: Medicinal chemistry perspectives, *Biochim. Biophys. Acta Rev. Cancer*, 2022, **1877**, 188725, DOI: 10.1016/j.bbcan.2022.188725.

16 J. Bogusz, K. Zrubek, K. P. Rembacz, P. Grudnik, P. Golik, M. Romanowska, B. Wladyka and G. Dubin, Structural analysis of PIM1 kinase complexes with ATP-competitive inhibitors, *Sci. Rep.*, 2017, **7**, 13399, DOI: 10.1038/s41598-017-13557-z.

17 L. S. Chen, S. Redkar, D. Bearss, W. G. Wierda and V. Gandhi, Pim kinase inhibitor, SGI-1776, induces apoptosis in chronic lymphocytic leukemia cells, *Blood*, 2009, **114**, 4150–4157, DOI: 10.1182/blood-2009-03-212852.

18 E. K. Keeton, K. McEachern, K. S. Dillman, S. Palakurthi, Y. Cao, M. R. Grondine, S. Kaur, S. Wang, Y. Chen, A. Wu, M. Shen, F. D. Gibbons, M. L. Lamb, X. Zheng, R. M. Stone, D. J. DeAngelo, L. C. Platanias, L. A. Dakin, H. Chen, P. D. Lyne and D. Huszar, AZD1208, a potent and selective pan-Pim kinase inhibitor, demonstrates efficacy in preclinical models of acute myeloid leukemia, *Blood*, 2014, **123**, 905–913, DOI: 10.1182/blood-2013-04-495366.

19 T. Paíno, A. Garcia-Gomez, L. González-Méndez, L. San-Segundo, S. Hernández-García, A.-A. López-Iglesias, E. M. Algarín, M. Martín-Sánchez, D. Corbacho, C. Ortiz-de-Solorzano, L. A. Corchete, N. C. Gutiérrez, M.-V. Maetos, M. Garayoa and E. M. Ocio, The Novel Pan-PIM kinase inhibitor, PIM447, displays dual antimyeloma and bone-protective effects, and potently synergizes with current standards of care, *Clin. Cancer Res.*, 2017, **23**, 225–238, DOI: 10.1158/1078-0432.CCR-16-0230.

20 H. Koblish, Y. Li, N. Shin, L. Hall, Q. Wang, K. Wang, M. Covington, C. Marando, K. Bowman, J. Boer, K. Burke, R. Wynn, A. Margulis, G. W. Reuther, Q. T. Lambert, V. Dostalik Roman, K. Zhang, H. Feng, C.-B. Xue, S. Diamond, G. Hollis, S. Yeleswaram, W. Yao, R. Huber, K. Vaddi and P. Scherle, Preclinical characterization of INCB053914, a novel pan-PIM kinase inhibitor, alone and in combination with anticancer agents, in models of hematologic malignancies, *PLoS ONE*, 2018, **13**, e0199108, DOI: 10.1371/journal.pone.0199108.

21 V. S. Walhekar, C. Bagul, D. Kumar and R. Kulkarni, Computational modelling strategies in exploring triazolopyridazine PIM1 kinase inhibitors as anticancer agents, *Anti-Cancer Agents Med. Chem.*, 2025, **25**(13), 954–966, DOI: 10.2174/1871520622666220820090353.

22 A. Choudhary, M. Khandekar, C. Bagul, A. Muthal and R. Kulkarni, Investigation of structure activity relationship: in silico studies of [1,2,4]triazolo[4,3-a]pyridine ureas as P38 kinase inhibitors, *Struct. Chem.*, 2023, **34**, 915–929, DOI: 10.1007/s11224-022-02046-3.

23 G. K. Ravindra, G. Achaiah, S. Laufer and V. M. Chandrashekar, Synthesis, anti-inflammatory and p38 kinase inhibitory activity of N, N′-diaryl urea derivatives, *Med. Chem.*, 2013, **9**, 213–221, DOI: 10.2174/1573406411309020006.

24 G. K. Ravindra, G. Achaiah, S. Laufer and V. M. Chandrashekar, Synthesis, p38 kinase inhibitory and anti-inflammatory activity of new substituted benzimidazole derivatives, *Med. Chem.*, 2013, **9**, 90–99, DOI: 10.2174/157340613804488440.

25 R. Kulkarni, U. Mitkari, S. Divyani, G. Achaiah, S. Laufer, D. V. R. N. Bikshapti, V. M. Chandrashekar, P. Gurav and S. J. Joshi, Design, synthesis, anti-inflammatory, p38 kinase inhibitory, antimicrobial and antitubercular activities of substituted benzamides, *Mini Rev. Med. Chem.*, 2018, **18**(17), 1486–1497, DOI: 10.2174/1389557517666170707105416.

26 S. Kulkarni, S. Deshpande, M. Shetty, P. Sahare, V. Shinde, A. Patil, V. Walhekar, S. G. Alegaon, S. D. Ranade, S. patrudu, A. Ganeshpurkar and R. Kulkarni, 2-Substituted 3-oxindoles as glycogen synthase kinase 3β inhibitors: Insights from ML based QSAR, molecular docking, and dynamics simulations, *Proc. Indian Natl. Sci. Acad.*, 2025, DOI: 10.1007/s43538-025-00533-9.

27 D. Anuradha, G. K. Ravindra, G. Achaiah and P. Radhakrishna, Pyrazole derivatives as potent inhibitors of c-Jun N-terminal kinase: synthesis and SAR studies,

Bioorg. Med. Chem., 2014, **22**, 6209–6219, DOI: 10.1016/j.bmc.2014.08.028.

28 G. N. D. Ion, G. M. Nitulescu and D. P. Mihai, A PIM-1 Kinase Inhibitor Docking Optimization Study Based on Logistic Regression Models and Interaction Analysis, *Life*, 2023, **13**(8), 1635, DOI: 10.3390/life13081635.

29 H. Park, J. Jeon, K. Kim, S. Choi and S. Hong, Structure-Based Virtual Screening and De Novo Design of PIM1 Inhibitors with Anticancer Activity from Natural Products, *Pharmaceuticals*, 2021, **14**(3), 275, DOI: 10.3390/ph14030275.

30 H. Almukadi, G. A. Jadkarim, A. Mohammed, M. Almansouri, N. Sultana, N. A. Shaik and B. Banaganapalli, Combining machine learning and structure-based approaches to develop oncogene PIM kinase inhibitors, *Front. Chem.*, 2023, **11**, 1137444, DOI: 10.3389/fchem.2023.1137444.

31 V. Walhekar, A. Muthal, M. Ghaisas, N. R. Mamidipalli, R. Kulkarni and R. Kulkarni, Reconnecting new tetrahydrobenzothieno-4-pyrimidine amides as potent PIM-1 kinase inhibitors via an integrated ligand and structure based scaffold hopping: In vitro anti-tumor investigations, *Bioorg. Chem.*, 2026, 109487, DOI: 10.1016/j.bioorg.2026.109487.

32 M. S. Sunkara, V. Kuchana, J. P. Sree, R. Prabugari, A. Pilli, F. Irum, S. J. Tangeda and D. Bhowmik, Pharmacophore-based virtual screening & molecular docking studies on selected plant constituents of Plantago major, *J. Applied Pharm. Sci.*, 2022, 157–167, DOI: 10.7324/JAPS.2023.92723.

33 D. Bajusz, A. Rácz and K. Héberger, Why is Tanimoto index an appropriate choice for fingerprint-based similarity calculations?, *J. Cheminf.*, 2015, 7(20), DOI: 10.1186/s13321-015-0069-3.

34 J. van Meerloo, G. J. L. Kaspers and J. Cloos, in. *Cell Sensitivity Assays: the MTT Assay*,2011, pp. 237–245, DOI: 10.1007/978-1-61779-080-5_20.

35 V. J. Sawant, S. R. Bamane, R. V. Shejwal and S. B. Patil, Comparison of drug delivery potentials of surface functionalized cobalt and zinc ferrite nanohybrids for curcumin in to MCF-7 breast cancer cells, *J. Magn. Magn. Mater.*, 2016, **417**, 222–229, DOI: 10.1016/j.jmmm.2016.05.061.

36 B. J. Alves, D. Ph, S. A. Goueli, D. Ph, H. Zegzouti, D. Ph, P. Corporation, PIM1 Kinase Assay, (n.d.) 1–2.

37 I. Lakshmanan and S. Batra, Protocol for Apoptosis Assay by Flow Cytometry Using Annexin V Staining Method, *Bio-protoc.*, 2013, **3**, 374, DOI: 10.21769/BioProtoc.374.

38 S. Martínez-González, S. Rodríguez-Arístegui, C. A. Gómez de la Oliva, A. I. Hernández, E. González Cantalapiedra, C. Varela, A. B. García, O. Rabal, J. Oyarzabal, J. R. Bischoff, J. Klett, M. I. Albarrán, A. Cebriá, N. Ajenjo, B. García-Serelde, E. Gómez-Casero, M. Cuadrado-Urbano, D. Cebrián, C. Blanco-Aparicio and J. Pastor, Discovery of novel triazolo[4,3-b]pyridazin-3-yl-quinoline derivatives as PIM inhibitors, *Eur. J. Med. Chem.*, 2019, **168**, 87–109, DOI: 10.1016/j.ejmech.2019.02.022.

39 O. Trott and A. J. Olson, AutoDock Vina: Improving the speed and accuracy of docking with a new scoring function, efficient optimization, and multithreading, *J. Comb. Chem.*, 2010, **31**, 455–461, DOI: 10.1002/jcc.21334.

40 R. Choudhary, V. Walhekar, A. Muthal, D. Kumar, C. Bagul and R. Kulkarni, Machine learning facilitated structural activity relationship approach for the discovery of novel inhibitors targeting EGFR, *J. Biomol. Struct. Dyn.*, 2023, 12445–12463, DOI: 10.1080/07391102.2023.2175263.

41 K. Mangala, W. Vinayak, C. Aasiya, B. Chandrakant, M. Amol, D. Kumar and R. Kulkarni, Reconnoitering imidazopyridazines as anticancer agents based on virtual modelling approach: quantitative structure activity relationship, molecular docking and molecular dynamics, *J. Biomol. Struct. Dyn.*, 2024, **42**, 2392–2409, DOI: 10.1080/07391102.2023.2204502.

42 S. Jagannath, W. Vinayak, M. Amol, P. Sandhya, V. M. Chandrashekhar, S. Vaibhav and R. Kulkarni, Molecular dynamics directed neuroprotective activity of alcoholic extract of Garuga pinnata Roxb. in Experimental Rats, *J. Ayurveda Integr. Med.*, 2025, **16**, 101032, DOI: 10.1016/j.jaim.2024.101032.

43 D. E. V. Pires, T. L. Blundell and D. B. Ascher, pkCSM: Predicting small-molecule pharmacokinetic and toxicity properties using graph-based signatures, *J. Med. Chem.*, 2015, **58**, 4066–4072, DOI: 10.1021/acs.jmedchem.5b00104.

44 A. Daina, O. Michielin and V. Zoete, SwissADME: a free web tool to evaluate pharmacokinetics, drug-likeness and medicinal chemistry friendliness of small molecules, *Sci. Rep.*, 2017, **7**, 42717, DOI: 10.1038/srep42717.